Journal of Theoretical Biology 444 (2018) 93–99

Contents lists available at ScienceDirect

Journal of Theoretical Biology

journal homepage: www.elsevier.com/locate/jtbi

Modeling factors that regulate cell cooperativity in the zebrafish posterior lateral line primordium

Leif Zinn-Björkman[a,*], Frederick R. Adler[a,b]

[a] Department of Mathematics, University of Utah, Salt Lake City, UT 84112, United States
[b] School of Biology, University of Utah, Salt Lake City, UT 84112, United States

ARTICLE INFO

Article history:
Received 31 December 2017
Revised 9 February 2018
Accepted 12 February 2018
Available online 20 February 2018

Keywords:
Collective migration
Receptor-ligand interaction
Chemotaxis
Gradient
Traveling wave

ABSTRACT

Collective cell migration is an integral part of organismal development. We consider migration of the zebrafish primordium during development of the posterior lateral line, a sensory system that detects water movement patterns. Experiments have shown that the chemokine ligand CXCL12a and its receptors CXCR4b and CXCR7b are key players for driving migration of the primordium, while FGF signaling helps maintain cohesion. In this work, we formulate a mathematical model of a laser ablated primordium separated into two smaller cell collectives: a leading collective that responds to local CXCL12a levels and a trailing collective that migrates up a local FGF gradient. Our model replicates recent experimental results, while also predicting a "runaway" behavior when FGF gradient response is inhibited. We also use our model to estimate diffusion coefficients of CXCL12a and FGF in the lateral line.

1. Introduction

Collective cell migration is an essential process during organismal development. Put simply, groups of cells need to be transported to specific locations in order to perform specific functions (Weijer, 2009). Often, cells require a chemical signal to guide their movement (chemotaxis). For example, chick neural crest cells are guided by growth factors, melanoma cells are guided by lysophosphatic acid (LPA), and *Dictyostelium* cells aggregate by secreting and following gradients of cyclic AMP (Ferguson et al., 2016; Tweedy et al., 2016; Weijer, 2009). Although collective cell migration has been studied extensively in these and other contexts, many open questions remain, including:

- How are signaling gradients formed and maintained by migrating cells?
- How do cells "read" signaling gradients?
- Do all cells in a collective sense a chemotactic signal, or do only leader cells sense the signal and direct follower cells?

The zebrafish posterior lateral line, a sensory network that detects water movement patterns, is an excellent system for studying the mechanisms that drive collective cell migration. Crucial to development of the lateral line is directed migration of the zebrafish posterior lateral line primordium, a collective of about 100 cells that migrates from the otic vesicle at the head of the fish to the tip of the tail along the horizontal myoseptum, a midbody tissue layer (Ghysen and Dambly-Chaudière, 2007). As it moves, the primordium periodically deposits rosette-shaped neuromasts, mechanosensory organs made up of a central hair cell surrounded by support cells. The lateral line is composed of 4–5 neuromasts along the surface of the body and 2–3 neuromasts at the tip of the tail (Aman and Piotrowski, 2011).

Movement of the primordium is driven by the chemokine ligand CXCL12a, also known as SDF1α, and its receptors CXCR4b and CXCR7b. The primordium follows a narrow stripe of CXCL12a expressed by muscle pioneer cells of the myoseptum (Li et al., 2004). CXCL12a is initially uniformly expressed along this stripe (Chitnis et al., 2012). Directed movement requires interaction of CXCL12a with CXCR4b and CXCR7b. CXCR4b is primarily expressed by leading (caudal) cells of the primordium during migration, while CXCR7b is primarily expressed by trailing (rostral) cells (Chitnis et al., 2012; Haas and Gilmour, 2006; Valentin et al., 2007). This polarized expression is believed to determine directed migration of the primordium, since the two receptors respond to CXCL12a in different ways. CXCR4b responds to CXCL12a with protrusive activity and directed migration (Luker et al., 2010). By contrast, when CXCL12a interacts with CXCR7b, no protrusions are observed, but CXCL12a is internalized and degraded (Chitnis et al., 2012). Although internalization of CXCL12a by either CXCR4b or CXCR7b results in intracellular degradation of CXCL12a, CXCR7b has a considerably higher binding affinity (Naumann et al., 2010). Thus, it is hypothesized that CXCR7b acts as a scavenger or sink for

* Corresponding author.
E-mail address: lzinnbj@math.utah.edu (L. Zinn-Björkman).

https://doi.org/10.1016/j.jtbi.2018.02.009
0022-5193/

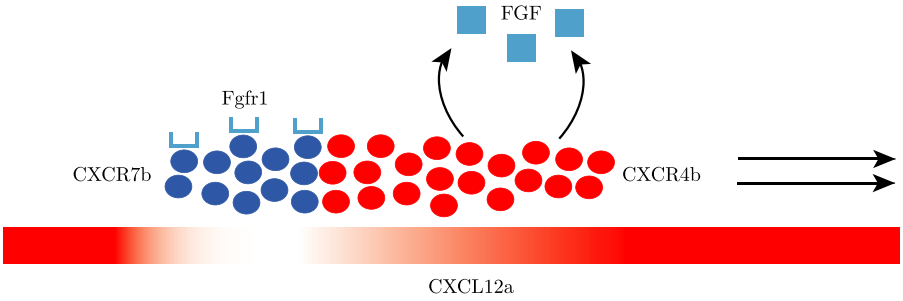

Fig. 1. Schematic of the factors that drive migration and cohesion of the primordium. Depletion of CXCL12a by trailing CXCR7b-expressing cells (blue) generates a local gradient of CXCL12a expression, which directs movement of leading CXCR4b-expressing cells (red). Trailing cells also express FGF receptor Fgfr1 and migrate toward FGF ligands secreted by leading cells. (For interpretation of the references to color in this figure legend, the reader is referred to the web version of this article.)

CXCL12a, substantially depleting ligand levels at the trailing end of the primordium. A local gradient of ligand is then created, with lower levels of CXCL12a at the trailing end of the primordium.

Experiments by Dalle Nogare et al. (2014) have given us insight into the cooperation of primordial cells during migration. Via laser ablation, the primordium was separated into two fragments, a small leading fragment containing only CXCR4b-expressing cells and a larger trailing fragment primarily containing CXCR7b-expressing cells. The purpose of this experiment was to determine if depletion of CXCL12a by trailing cells could create a broad enough depression in CXCL12a activity to polarize migration of the separated leading fragment. The result in most trials was that the leading fragment stalled shortly after ablation, and then stretched, indicating that CXCL12a clearance by trailing CXCR7b-expressing cells cannot bias migration of the leading fragment over long distances. However, the trailing fragment, after initially stalling, always resumed caudal migration toward the leading fragment. Eventually, the two fragments rejoined, and the entire primordium migrated cohesively. This behavior of the trailing fragment was observed even after introducing the CXCL12a inhibitor chalcone-4-hydrate, which shows that migration of the trailing cells is not driven by a polarized response to CXCL12a. Further experiments showed that FGF ligands secreted by leading cells act as a chemoattractant for trailing cells (Fig. 1).

1.1. Goals of this work

Two previous models have been developed to describe cell cooperativity during migration of the primordium. Dalle Nogare et al. (2014) developed an agent-based computational model of primordium migration inspired by their experimental findings. This model successfully replicates the authors' laser ablation experiments. Knutsdottir et al. (2017) developed a 3D deformable ellipsoid mathematical model in which leading cells sense gradients of CXCL12a and trailing cells sense gradients of FGF. The authors investigated how cell division, adhesion, and chemotaxis affect primordium migration. They also challenged the model to replicate the results from Dalle Nogare et al. (2014), and found good agreement with experiments and the previous computational model. Although these models successfully reproduce experimental results, they do not address CXCL12a and FGF concentration profiles in detail and are not analytically tractable.

In this work, we formulate a simpler mathematical model to study a laser ablated zebrafish primordium. This model concentrates on primordium migration - we do not include cell proliferation or cell differentiation. We model the laser ablated portions of the primordium as two regions, a leading region that responds to CXCL12a activity and a trailing region that migrates towards FGFs secreted within the leading region. For certain parameter values, this model replicates experimental results. We fit parameters in our model to cell-tracking data obtained from a laser ablation video, thereby obtaining estimates for CXCL12a and FGF diffusion coefficients in the zebrafish lateral line system. For some parameter values, however, the leading region "runs away" from the trailing region, a behavior roughly akin to a neuromast deposition, but not seen in experiments or in previous models. We investigate this runaway case by deriving traveling wave solutions for CXCL12a and FGF and searching for parameter values that make a cohesive traveling wave solution impossible to obtain.

We begin by formulating the mathematical model, which consists of two partial differential equations (PDEs) for CXCL12a and FGF and two ordinary differential equations (ODEs) for rod positions as a function of time. We then discuss outcomes from simulations of the model and parameter fitting. Later, we derive traveling wave solutions for CXCL12a and FGF, as well as a self-consistency condition for velocity of the leading and trailing region. Finally, we use the traveling wave solutions we have obtained to investigate the self-consistency condition in more detail and discuss parameters that influence qualitative behavior of the model (runaway and cohesion).

2. The model

We model the primordium as two rigid rods, which represent the leading and trailing fragments created by Nogare et al. by laser ablation. This model is based on the following assumptions:

- CXCR4b and CXCR7b concentrations are constant in time.
- The expression domains for each receptor are distinct - the leading fragment expresses only CXCR4b and the trailing fragment expresses only CXCR7b.
- The leading and trailing fragments are the same length.
- Cells in each fragment internalize and degrade CXCL12a, with a tenfold higher degradation rate in the trailing CXCR7b-expressing fragment.
- Because primordium cells are flat and CXCL12a is expressed in a thin stripe, we reduce to one dimension. We model the boundaries of the domain as impermeable (no flux).

2.1. PDEs for ligands

Each rod has length $2l$; the leading rod has center of mass at c_1 and expresses only CXCR4b (R_4), while the trailing rod has center of mass at c_2 and expresses only CXCR7b (R_7). Within the bounds of the leading rod, CXCL12a is co-internalized and degraded by CXCR4b at a rate ρ_4. Within the trailing rod, CXCL12a is co-internalized and degraded by CXCR7b at rate ρ_7. CXCL12a is also secreted at a uniform rate in the entire domain $x \in [0, N]$. It also diffuses and undergoes natural decay. Thus, the equation for CXCL12a is

$$L_t = \alpha_L - \delta_L L - I(x - c_1)\rho_4 R_4 L - I(x - c_2)\rho_7 R_7 L + D_L L_{xx}, \qquad (1)$$

$$L(x,0) = L_0, \quad L_x(0,t) = L_x(N,t) = 0, \tag{2}$$

where

$$I(x) = \begin{cases} 1 & \text{if} |x| \le l, \\ 0 & \text{otherwise.} \end{cases}$$

The cells in the leading fragment secrete FGF ligands, which act as a chemoattractive cue for the cells in the trailing fragment. Thus, the equation for FGF (G) is

$$G_t = I(x - c_1)\alpha_G - \delta_G G + D_G G_{xx}, \tag{3}$$

$$G(x,0) = 0, \quad G_x(0,t) = G_x(N,t) = 0, \tag{4}$$

where α_G and δ_G are production and natural decay rates of FGF, respectively, and D_G is the FGF diffusion coefficient. We do not include additional FGF degradation within the trailing rod because we assume that FGF ligands are rapidly internalized and recycled by trailing cells.

2.2. ODEs for rod positions

Experiments on a cohesive (unablated) primordium show that the absolute level of CXCL12a determines the migratory response (Dalle Nogare et al., 2014). With this in mind, we assume that cells are pulling at each end of the leading rod with force proportional to local CXCL12a expression. Thus, we model velocity of the leading rod as proportional to the absolute difference in CXCL12a concentration between its front edge and back edge. Less is known about the mechanism of FGF chemotaxis; we assume that trailing rod velocity is proportional to the average gradient of FGF within the rod. Following these assumptions, we have

$$c_1'(t) = \sigma_L(L(c_1 + l, t) - L(c_1 - l, t)), \tag{5}$$

$$c_2'(t) = \sigma_G \frac{G(c_2 + l, t) - G(c_2 - l, t)}{2l}, \tag{6}$$

where σ_L and σ_G are CXCL12a protrusive response and FGF gradient response, respectively. In simulations, the leading and trailing rods are given an initial separation l_0, i.e.,

$$c_1(0) = c_2(0) + 2l + l_0. \tag{7}$$

3. Numerical simulation and parameter fitting

To numerically simulate the model specified by Eqs. (1)–(6), we used Forward Euler scheme to discretize time and Crank–Nicolson scheme for diffusion terms. To estimate unknown parameter values, we tracked positions of the leading cell in each fragment frame-by-frame from supplementary movie S3 in Dalle Nogare et al. (2014) (doi:10.1242/dev.106690). We observed the following:

- The trailing fragment is stationary for approximately one hour before it begins migration toward the leading fragment. This may indicate that FGF ligands secreted by leading cells take about an hour to diffuse into the trailing domain, allowing us to estimate the FGF diffusion coefficient. This diffusion time estimate is an upper bound, however, since it assumes that the stalling of the trailing fragment is unrelated to potential damage caused by laser ablation and that trailing cells can instantly respond to local FGF expression.
- After initiation of trailing fragment migration at one hour, it takes another hour for the two fragments to rejoin. This allows us to estimate FGF gradient response.
- After the fragments rejoin, migration velocity of entire collective is roughly constant, and similar to velocity of the trailing fragment alone ($\sim$1.1 μm/min.).

Default parameter values are specified in Table 1.

Fig. 2 displays three frames from simulation of an ablated primordium, after 1, 2, and 3 h. At 1 h, CXCR7b has already substantially depleted CXCL12a levels in the trailing rod, but, due to limited CXCL12a diffusion, this has not affected CXCL12a levels in the separated leading rod. CXCL12a activity remains unpolarized in the leading rod, which remains stationary. However, FGF ligands have diffused to the trailing rod, which has begun to migrate toward the leading rod. At 2 h, the trailing rod has joined the leading rod, and CXCL12a activity within the primordium is now polarized. The primordium can now begin to migrate cohesively. At 3 h, the primordium is moving at constant velocity. In simulations, we assume that once the trailing rod meets the leading rod, they adhere to one another and subsequently migrate as a unit. Position with time from this simulation agrees well with time course data obtained from Dalle Nogare et al. (2014) (see Fig. 4A).

What happens when FGF gradient response is inhibited? In Fig. 3, we show three frames from a simulation with σ_G reduced by a factor of ten and every other parameter unchanged. In this scenario, the trailing rod eventually migrates close enough to the leading rod to polarize CXCL12a expression levels within the leading rod, but not close enough to rejoin the leading rod. The leading rod then migrates away from the trailing rod, meaning that the trailing rod encounters lower and lower FGF levels over time. Hence, the trailing rod stalls, while the leading rod continues to migrate at constant velocity. Interestingly, this runaway behavior occurs regardless of the initial rod separation distance. Long-term migration velocity of the leading rod is also uninfluenced by initial separation (Fig. 4B).

We have observed two qualitative behaviors in simulation, a “cohesive” case in which the rods reach the same limiting velocity and a runaway case in which the leading rod reaches a nonzero steady-state velocity and the trailing rod stalls. To investigate these cases further, we seek constant velocity traveling wave solutions to (1) and (3).

4. Traveling wave solutions

To reduce the number of parameters and simplify computations, we begin by nondimensionalizing the model equations, as follows:

$$\mathscr{L}_\tau = 1 - \delta\mathscr{L} - I(y - C_1)r_4\mathscr{L} - \tilde{I}(y - C_2)r_7\mathscr{L} + d_L\mathscr{L}_{yy}, \tag{8}$$

$$g_\tau = I(y - C_1) - g + d_G g_{yy}, \tag{9}$$

where

$$\tau = \delta_G t, \quad y = \frac{x}{l}, \quad C_1 = \frac{c_1}{l}, \quad C_2 = \frac{c_2}{l}, \quad \mathscr{L} = \frac{\delta_G}{\alpha_L}L, \quad g = \frac{\delta_G}{\alpha_G}G,$$

$$r_4 = \frac{\rho_4}{\delta_G}R_4, \quad r_7 = \frac{\rho_7}{\delta_G}R_7, \quad \delta = \frac{\delta_L}{\delta_G}, \quad d_L = \frac{D_L}{\delta_G l^2}, \quad d_G = \frac{D_G}{\delta_G l^2},$$

and

$$\tilde{I}(y) = \begin{cases} 1 & \text{if } |y| \le 1, \\ 0 & \text{otherwise.} \end{cases}$$

The equations for C_1 and C_2 are given by

$$C_1'(\tau) = s_L(\mathscr{L}(C_1 + 1, \tau) - \mathscr{L}(C_1 - 1, \tau)), \tag{10}$$

$$C_2'(\tau) = s_G(g(C_2 + 1, \tau) - g(C_2 - 1, \tau)), \tag{11}$$

Table 1
Model parameters. Receptor concentrations were chosen to generate reasonable amounts of CXCL12a degradation within the leading and trailing rods. Ligand production rates were chosen to scale with protrusive and gradient response.

Parameter	Definition	Value	References
l	Rod lengths (x0.5)	30 µm	Dalle Nogare et al. (2014)
α_L	L12a production rate	0.03 nM min^{-1}	Assumed
δ_L	L12a natural decay	0.03 min^{-1}	Misra et al. (2008)
R_4, R_7	Receptor concentrations	1 nM	Assumed
ρ_7	L12a-R7b binding rate	$2.8 \cdot 10^6$ M^{-1} s^{-1}	Est. from Rich et al. (2002)
ρ_4	L12a-R4b binding rate	$2.8 \cdot 10^5$ M^{-1} s^{-1}	10x smaller than ρ_7
D_L	L12a diffusion coefficient	2 μm^2 min^{-1}	Fit to data
α_G	FGF production rate	0.03 nM min^{-1}	Assumed
δ_G	FGF natural decay	0.015 min^{-1}	Khosravi et al. (2007)
D_G	FGF diffusion coefficient	4 μm^2 min^{-1} mm^2/h	Fit to data
σ_L	Protrusive response to L12a	2.5 µm nM^{-1} min^{-1}	Fit to data
σ_G	FGF gradient response	350 μm^2 nM^{-1} min^{-1}	Fit to data

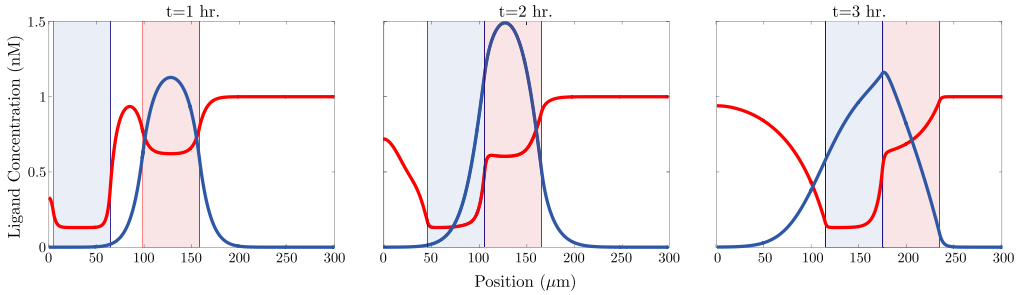

Fig. 2. Three frames from simulation with an initial separation of 35 µm. CXCL12a expression is indicated by red curve and FGF expression by blue curve. Leading rod (red shaded region) responds to CXCL12a activity and trailing rod (blue shaded region) to FGF activity. (For interpretation of the references to color in this figure legend, the reader is referred to the web version of this article.)

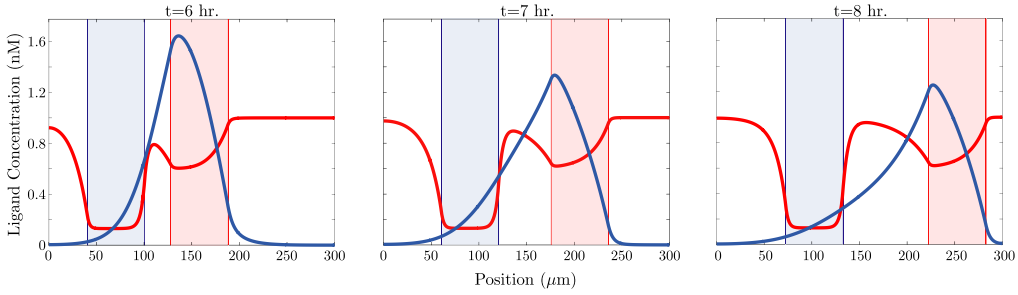

Fig. 3. Three frames from simulation with reduced FGF gradient response ($\sigma_G = 35$). CXCL12a, FGF, and leading/trailing regions are represented by the same conventions as Fig. 2. Trailing rod approaches leading rod, then stalls, while leading rod migrates away.(For interpretation of the references to color in this figure legend, the reader is referred to the web version of this article.)

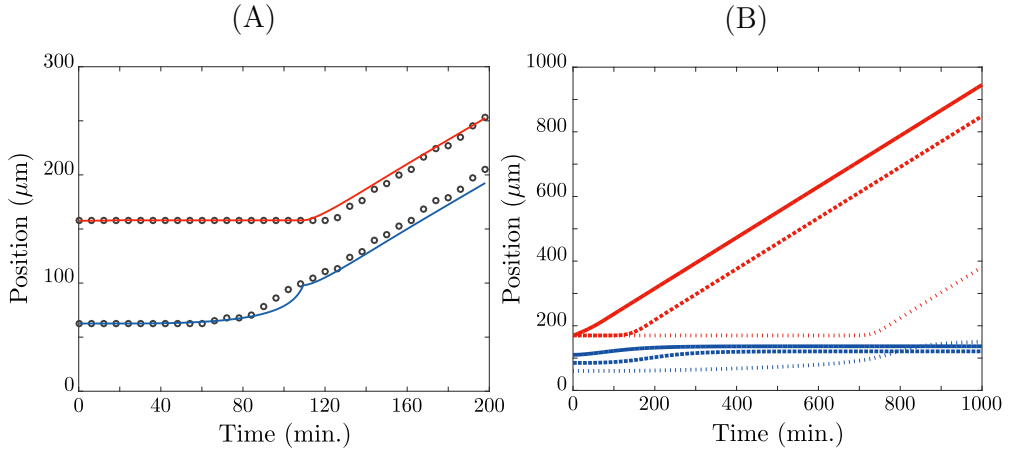

Fig. 4. (A) Comparison of time course data for numerical simulation and laser ablation experiment (circles), using parameters specified in Table 1. (B) Time course data for runaway case, with initial separation 0, 25, and 50 µm (solid, dashed, and dotted lines, respectively). Red curves represent the leading rod and blue curves represent the trailing rod. (For interpretation of the references to color in this figure legend, the reader is referred to the web version of this article.)

where

$$s_L = \frac{\sigma_L \alpha_L}{\delta_G^2 l} \text{ and } s_G = \frac{\sigma_G \alpha_G}{2\delta_G^2 l^2}.$$

Now, let $\xi = y - C_1$ be the traveling wave coordinate, with $C_1' = C_2' = v$.

4.1. FGF traveling wave profile

We designate three regions: behind the leading rod (1), within the leading rod (2), and ahead of the leading rod (3). In regions (1) and (3), we have

$$-vg'(\xi) = -g(\xi) + d_G g''(\xi). \tag{12}$$

This has solution

$$g^{(1,3)}(\xi) = A^{(1,3)} \exp(\lambda_+ \xi) + B^{(1,3)} \exp(\lambda_- \xi), \tag{13}$$

where $\lambda_\pm = \left(-v \pm \sqrt{v^2 + 4d_G}\right)/(2d_G)$. In region (2), we obtain

$$-vg'(\xi) = 1 - g(\xi) + d_G g''(\xi), \tag{14}$$

which gives

$$g^{(2)}(\xi) = 1 + A^{(2)} \exp(\lambda_+ \xi) + B^{(2)} \exp(\lambda_- \xi). \tag{15}$$

The FGF traveling wave profile must go to steady state as $\xi \to \pm\infty$, so we require that

$$\lim_{\xi \to -\infty} \frac{dg^{(1)}}{d\xi} = 0 \text{ and } \lim_{\xi \to +\infty} \frac{dg^{(3)}}{d\xi} = 0.$$

Thus, $B^{(1)} = A^{(3)} = 0$. To solve for the remaining constants, we require continuity of g and g' at the boundaries of the leading rod ($\xi = -1$ and $\xi = 1$). This gives

$$A^{(1)} = e^{\lambda_+} + \frac{1}{\lambda_+ - \lambda_-}(\lambda_- e^{-\lambda_+} - \lambda_+ e^{\lambda_+}), \quad A^{(2)} = \frac{\lambda_-}{\lambda_+ - \lambda_-} e^{-\lambda_+},$$

$$B^{(2)} = \frac{-\lambda_+}{\lambda_+ - \lambda_-} e^{\lambda_-}, \quad B^{(3)} = e^{-\lambda_-} + \frac{1}{\lambda_+ - \lambda_-}(\lambda_- e^{-\lambda_-} - \lambda_+ e^{\lambda_-}).$$

4.2. CXCL12a traveling wave profile

We proceed in a similar manner to find the traveling wave profile for CXCL12a. Because CXCL12a is degraded more rapidly within the trailing rod than within the leading rod, we now have five regions:

(1) Behind the trailing rod: $\xi < -(3 + \xi_0)$,
(2) Within the trailing rod: $-(3 + \xi_0) \le \xi \le -(1 + \xi_0)$,
(3) Between the rods: $-(1 + \xi_0) < \xi < -1$,
(4) Within the leading rod: $-1 \le \xi \le 1$,
(5) Ahead of the leading rod: $\xi > 1$, where ξ_0 is the rod separation. Solving the ODEs for $\mathscr{L}(\xi)$ in each region and requiring that

$$\lim_{\xi \to -\infty} \frac{d\mathscr{L}^{(1)}}{d\xi} = \lim_{\xi \to +\infty} \frac{d\mathscr{L}^{(5)}}{d\xi} = 0,$$

we obtain

$$\mathscr{L}^{(1)}(\xi) = \frac{1}{\delta} + A^{(1)} \exp(\mu_+ \xi), \tag{16}$$

$$\mathscr{L}^{(2)}(\xi) = \frac{1}{\delta + r_7} + A^{(2)} \exp(\mu_+ \xi) + B^{(2)} \exp(\mu_- \xi), \tag{17}$$

$$\mathscr{L}^{(3)}(\xi) = \frac{1}{\delta} + A^{(3)} \exp(\mu_+ \xi) + B^{(3)} \exp(\mu_- \xi), \tag{18}$$

$$\mathscr{L}^{(4)}(\xi) = \frac{1}{\delta + r_4} + A^{(4)} \exp(\mu_+ \xi) + B^{(4)} \exp(\mu_- \xi), \tag{19}$$

$$\mathscr{L}^{(5)}(\xi) = \frac{1}{\delta} + B^{(5)} \exp(\mu_- \xi), \tag{20}$$

where $\mu_\pm = \left(-v \pm \sqrt{v^2 + 4d_L(\delta + \tilde{r}_4 + \tilde{r}_7)}\right)/(2d_L)$. Here, $\tilde{r}_4 = r_4$ in region (4) and 0 everywhere else and $\tilde{r}_7 = r_7$ in region (2) and 0 elsewhere. We can find the arbitrary constants by requiring continuity in $\mathscr{L}$ and $\mathscr{L}'$ and numerically solving a linear system of equations.

The rod separation ξ_0 and rod velocity v must be chosen to satisfy the following self-consistency requirement:

$$v = s_L[\mathscr{L}(1, v) - \mathscr{L}(-1, v)] = s_G[g(-(1 + \xi_0), v) - g(-(3 + \xi_0), v)]. \tag{21}$$

Solutions to (21) represent the steady state rod separation and velocity obtained by our model for a given choice of parameters. For sample FGF and CXCL12a traveling wave profiles, see Fig. 5.

4.3. Runaway versus synchronized migration

We want to search parameter space for values of ξ_0 and v that satisfy (21). To do this, we plot leading rod velocity and trailing rod velocity as a function of rod separation and look for points of intersection. See Fig. 6 for a plot with three different values of σ_G, the FGF gradient response. For $\sigma_G = 300$, we have two intersections, at (3.4 µm, 1.6 µm/s) and (35.7 µm, 1.4 µm/s). The first intersection corresponds to a "stable" traveling wave solution and agrees with numerical simulation of the model, while the second intersection corresponds to an "unstable" traveling wave solution that is not observed in simulations. In the unstable case, a small perturbation reducing rod separation results in convergence to the stable solution, while a small perturbation increasing rod separation results in runaway. For $\sigma_G = 270$, we also have two intersections, at (5.3 µm, 1.5 µm/s) and (25.4 µm, 1.4 µm/s). Again, only the first separation and velocity are observed in simulations. For $\sigma_G = 240$, there are no intersections, meaning that a self-consistent solution does not exist. The leading rod velocity curve always lies above the trailing rod velocity curve, indicating that the leading rod runs away from the trailing rod. This agrees with numerical simulation, which shows that the leading rod assumes a constant velocity and separates from the trailing rod, which eventually stalls. This behavior is reminiscent of a neuromast deposition.

5. Discussion

In this work, we have proposed a chemotactic model of cell cooperation in the zebrafish primordium. The mechanisms that drive migration in our model are the chemoattractants CXCL12a and FGF, as well as spatial polarity in the expression of the CXCL12a receptors CXCR4b and CXCR7b. For a range of parameter values, our model agrees qualitatively with experiments: FGFs help maintain cohesion in an unablated primordium and rescue migration in an ablated primordium. In simulations of an ablated primordium, we observe that the leading region initially stalls, the trailing region rejoins the leading region, and the two regions eventually migrate cohesively (at the same velocity). For low levels of FGF gradient response, however, our model displays behavior not seen in ablation experiments: the trailing region migrates close enough to polarize CXCL12a expression within the leading region, whereupon the leading region runs away from the trailing region.

This runaway case is particularly interesting because it illuminates possible mechanisms behind neuromast deposition, in which part of the primordium is left behind the cohesive migrating portion. The leading region separates from the trailing region when we reduce non-dimensional FGF gradient response $s_G =$

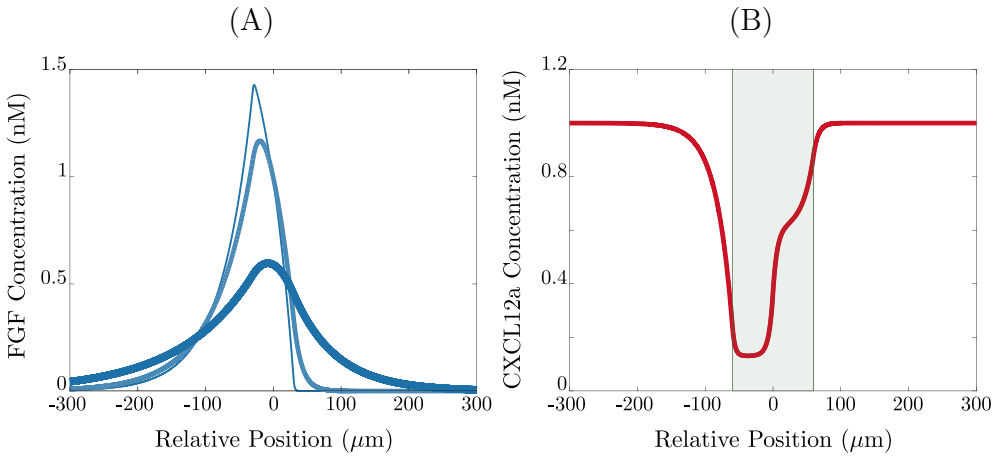

Fig. 5. (A) FGF traveling wave profile for varying FGF diffusion coefficients (1, 10, 100 μm^2/min.). Line thickness increases as diffusion coefficient is increased. Bounds of the leading rod, where FGF is produced, are −30 μm–30 μm. (B) CXCL12a traveling wave profile (red curve) with diffusion coefficient 5 μm^2/min. for a cohesive traveling wave solution (separation 0 μm). Shaded region indicates the location of the primordium, where the center of mass is located at the origin. (For interpretation of the references to color in this figure legend, the reader is referred to the web version of this article.)

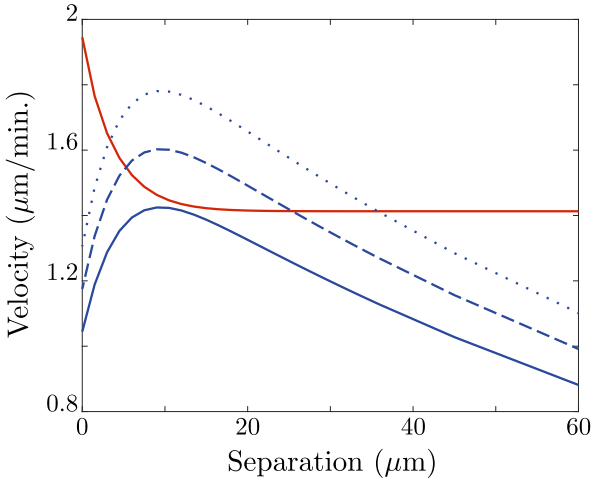

Fig. 6. Rod separation vs. rod velocity. Red curve is leading rod speed, blue curves are trailing rod speeds for various σ_G (dotted line: $\sigma_G = 300$, dashed line: $\sigma_G = 270$, solid line: $\sigma_G = 240$). Intersections between curves correspond to self-consistent traveling wave solutions. Limiting value of red curve represents asymptotic velocity of the leading rod in the runaway case. (For interpretation of the references to color in this figure legend, the reader is referred to the web version of this article.)

$(\sigma_G \alpha_G)/(2\delta_G^2 l^2)$ below some critical level. α_G and δ_G, the production and natural decay rates of FGF, respectively, are likely unchanged throughout primordium migration. However, it is known that the length of the CXCR7b expression zone increases prior to a deposition, which decreases s_G (Aman and Piotrowski, 2011; Chitnis et al., 2012). Hence, neuromast deposition could be triggered when the trailing region reaches a critical length. Another possible mechanism is that σ_G, the response to FGF gradient, is inhibited prior to a deposition.

Aman and Piotrowski (2011) suggested that cells in the trailing CXCR7b zone express genes that promote neuromast deposition. The authors proposed three possible deposition mechanisms, possibly working in concert: the ability of trailing cells to migrate is inhibited, adhesion strength between trailing cells and the underlying substrate is increased, or adhesion strength between leading and trailing cells is decreased. Our model confirms that the first mechanism can generate neuromast depositions without stalling of the leading region, though it certainly does not disprove the other two hypotheses. More work will be needed to isolate the true mechanisms of neuromast deposition.

The runaway case could potentially be tested experimentally using the FGF receptor inhibitor SU5402. Dalle Nogare et al. (2014) confirmed that treatment of zebrafish embryos with SU5402 resulted in significantly less migration of the trailing fragment toward the leading fragment following laser ablation. If this experiment could be performed over a longer period, we could observe whether the trailing fragment eventually rejoins the leading fragment or if runaway of the leading fragment occurs. It would also be interesting to treat a cohesive primordium with SU5402 and observe whether or not the primordium separates. Simulations of our model predict that runaway behavior does not depend on initial separation; however, we do not account for adhesive connections between the leading and trailing region when initial separation is zero.

This work also examines primordium migration quantitatively. We analyzed a laser ablation video from the supplementary materials of Dalle Nogare et al. (2014). By examining the position of the leading cell in each fragment frame-by-frame, we were able to obtain estimates for the fragment separation distance, initial stalling period, time to rescue cohesion, and average migration velocity after the fragments rejoined. By observing the time it took for the trailing fragment to begin migration toward the leading fragment, we estimated the FGF diffusion coefficient in the lateral line. We were also able to obtain an estimate for the CXCL12a diffusion coefficient by fitting our model to video data. These estimates are somewhat smaller than the coefficients used in Knutsdottir et al. (2017), and almost four orders of magnitude smaller than the coefficients observed in water (Veldkamp et al., 2009). This suggests that efficient migration of the zebrafish primordium requires limited ligand diffusion.

It would be interesting to compare traveling waves profiles of CXCL12a and FGF obtained by our model with spatial distributions of these ligands in zebrafish embryos. Unfortunately, this is not possible at present, due to a lack of tools for visualizing signaling activity *in vivo*. A major issue is that fluorescent labels applied to attractants remain fluorescent when the attractants are broken down; hence, a self-generated attractant gradient (e.g., CXCL12a in the lateral line) would not be paralleled by a fluorescence gradient (Tweedy et al., 2016). Because of this complication, the CXCL12a local gradient hypothesis had to be verified indirectly, by compar-

ing CXCR4b lifetime ratios at the leading and trailing ends of the primordium (Donà et al., 2013).

In our model, we assume that the chemotactic response to CXCL12a and FGF is based on a "tug-of-war" mechanism, wherein the speed of the rods depends on levels of ligand at their leading and trailing ends. Another possible mechanism is that a constant positive migration speed is achieved when ligand levels eclipse a critical threshold at only one end. Future work could explore whether or not a threshold mechanism for migration changes the qualitative behavior of our model.

We are currently using our findings from this work to develop a model of migration and deposition of the zebrafish primordium. We have transitioned to an individual cell based approach, with leading cells guided by CXCL12a and trailing cells by FGFs. By incorporating cell proliferation, we can induce runaway of leading cells from trailing cells, as trailing cells are displaced into regions with lower expression levels of FGF. We hope to use this model to address how migration is affected by changing the proportions of cells that express CXCR4b and CXCR7b, how cell proliferation rate affects neuromast spacing, and which mechanisms control the number of deposited cells.

Competing interests

The authors have declared that no competing financial interests exist.

Acknowledgments

This work was supported by the National Science Foundation grant RTG-1148230.

References

Aman, A., Piotrowski, T., 2011. Cell-cell signaling interactions coordinate multiple cell behaviors that drive morphogenesis of the lateral line. Cell Adhes. Migration 5 (6), 499–508.

Chitnis, A.B., Dalle Nogare, D., Matsuda, M., 2012. Building the posterior lateral line system in zebrafish. Dev. Neurobiol. 72 (3), 234–255.

Dalle Nogare, D., Somers, K., Rao, S., Matsuda, M., Reichman-Fried, M., Raz, E., Chitnis, A.B., 2014. Leading and trailing cells cooperate in collective migration of the zebrafish posterior lateral line primordium. Development 141 (16), 3188–3196.

Donà, E., Barry, J.D., Valentin, G., Quirin, C., Khmelinskii, A., Kunze, A., Durdu, S., Newton, L.R., Fernandez-Minan, A., Huber, W., et al., 2013. Directional tissue migration through a self-generated chemokine gradient. Nature 503 (7475), 285.

Ferguson, E.A., Matthiopoulos, J., Insall, R.H., Husmeier, D., 2016. Inference of the drivers of collective movement in two cell types: Dictyostelium and melanoma. J. R. Soc. Interface 13 (123), 20160695.

Ghysen, A., Dambly-Chaudière, C., 2007. The lateral line microcosmos. Genes Dev. 21 (17), 2118–2130.

Haas, P., Gilmour, D., 2006. Chemokine signaling mediates self-organizing tissue migration in the zebrafish lateral line. Dev. Cell 10 (5), 673–680.

Khosravi, A., Cutler, C.M., Kelly, M.H., Chang, R., Royal, R.E., Sherry, R.M., Wodajo, F.M., Fedarko, N.S., Collins, M.T., 2007. Determination of the elimination half-life of fibroblast growth factor-23. J. Clin. Endocrinol. Metab. 92 (6), 2374–2377.

Knutsdottir, H., Zmurchok, C., Bhaskar, D., Palsson, E., Dalle Nogare, D., Chitnis, A.B., Edelstein-Keshet, L., 2017. Polarization and migration in the zebrafish posterior lateral line system. PLoS Comput. Biol. 13 (4), e1005451.

Li, Q., Shirabe, K., Kuwada, J.Y., 2004. Chemokine signaling regulates sensory cell migration in zebrafish. Dev. Biol. 269 (1), 123–136.

Luker, K.E., Steele, J.M., Mihalko, L.A., Ray, P., Luker, G.D., 2010. Constitutive and chemokine-dependent internalization and recycling of cxcr7 in breast cancer cells to degrade chemokine ligands. Oncogene 29 (32), 4599.

Misra, P., Lebeche, D., Ly, H., Schwarzkopf, M., Diaz, G., Hajjar, R.J., Schecter, A.D., Frangioni, J.V., 2008. Quantitation of cxcr4 expression in myocardial infarction using 99mtc-labeled sdf-1α. J. Nucl. Med. 49 (6), 963–969.

Naumann, U., Cameroni, E., Pruenster, M., Mahabaleshwar, H., Raz, E., Zerwes, H.-G., Rot, A., Thelen, M., 2010. Cxcr7 functions as a scavenger for cxcl12 and cxcl11. PloS one 5 (2), e9175.

Rich, R.L., Hoth, L.R., Geoghegan, K.F., Brown, T.A., LeMotte, P.K., Simons, S.P., Hensley, P., Myszka, D.G., 2002. Kinetic analysis of estrogen receptor/ligand interactions. Proc. Natl. Acad. Sci. 99 (13), 8562–8567.

Tweedy, L., Knecht, D.A., Mackay, G.M., Insall, R.H., 2016. Self-generated chemoattractant gradients: attractant depletion extends the range and robustness of chemotaxis. PLoS Biol. 14 (3), e1002404.

Valentin, G., Haas, P., Gilmour, D., 2007. The chemokine sdf1a coordinates tissue migration through the spatially restricted activation of cxcr7 and cxcr4b. Current Biol. 17 (12), 1026–1031.

Veldkamp, C.T., Ziarek, J.J., Su, J., Basnet, H., Lennertz, R., Weiner, J.J., Peterson, F.C., Baker, J.E., Volkman, B.F., 2009. Monomeric structure of the cardioprotective chemokine sdf-1/cxcl12. Protein Sci. 18 (7), 1359–1369.

Weijer, C.J., 2009. Collective cell migration in development. J. Cell. Sci. 122 (18), 3215–3223.